UNIVERSITÀ DEGLI STUDI DI PADOVA

Dipartimento di Fisica e Astronomia "Galileo Galilei"

Bachelor Degree in Physics

Final Dissertation

Energy calibration of the JUNO liquid scintillator test beam setup

Calibrazione in energia dell'apparato su fascio per lo studio dello scintillatore liquido di JUNO

Thesis supervisor

Prof. Alberto Garfagnini

Thesis co-supervisor

Dott. Arsenii Gavrikov

Candidate

Benedetta Rasera

Academic Year 2023/2024

Abstract

The Jiangmen Underground Neutrino Observatory (JUNO) is a large liquid scintillator neutrino detector under construction in South China. The main goal of the experiment is to measure the neutrino oscillation parameters with sub-percent precision and to determine the neutrino mass ordering at $3-4\sigma$ significance level after 6 years of data taking. The core of the experiment is a 35.4 m diameter spherical vessel filled with high purity, large mass (20 kton) liquid scintillator (LS) target. To achieve the physics goals, several challenges have been set, one of those is to study the properties of the liquid scintillator that will be employed during the experiment.

The original aim of this work has been to study the performances of the JUNO LS final recipe with test beam particles. An experiment has been designed by the JUNO group lead by Prof. Hans Steiger at the Tecnische Universität München (TUM) and installed in the beam line of the CN Van-der-Graff accelerator at the INFN National Laboratories in Legnaro (Padua, Italy). The experiment consisted in inserting a small LS setup on the proton beamline and measure the response of the JUNO LS to beam particles. I participated to the setting up of the apparatus and to the data taking shifts. The main topic of the thesis has been the analysis of the energy calibration data which were collected using three different gamma sources: ^{22}Na, ^{133}Ba and ^{137}Cs. I started with the investigation of the quality of the collected data, studying the signal baseline and the rising and falling times of the collected waveforms. Afterwards, I systematically investigated different algorithms for the charge reconstruction, selecting a suitable method. The final algorithm has been applied to the reconstruction of the radioactive sources and a calibration curve obtained. With the latter it has been possible to calibrate the proton beam data. The calibration curve will be used to correct the beam data and determine the energy distribution collected with the detector.

L'esperimento Jiangmen Underground Neutrino Obsevatory (JUNO) è un grande rivelatore a scintillatore liquido per la fisica dei neutrino attualmente in costruzione nella Cina meridionale. L'obiettivo principale dell'esperimento è misurare i parametri dell'oscillazione dei neutrini con una precisione inferiore al percento e determinare l'ordinamento della massa dei neutrini con un livello di significatività di $3-4\ \sigma$ in 6 anni di presa dati. Il nucleo dell'esperimento è una sfera di 35.4 m di diametro riempita con 20 kton si scintillatore liquido (LS) di elevata purezza e grande massa (20 kton). Per raggiungere gli obiettivi di fisica JUNO ha dovuto affrontare importanti sfide tecnologiche: le proprietà chimico-fisiche dello scintillatore sono un ingrediento importante per la riuscita dell'esperimento.

Lo scopo iniziale di questo lavoro era quello di studiare le caratteristiche della miscela finale dello scintillatore liquido di JUNO. Il gruppo JUNO della Technische Universität München, guidato dal Prof. Hans Steiger della Tecnische ha progettato ed installato sulla linea di fascio dell'acceleratore di Van-der-Graaf CN ai Laboratori Nazionali di Legnaro (Padova, Italia)

dell'INFN un esperimento per studiare la risposta dello scintillatore liquido a particelle del fascio di varia energia. Dopo aver preso parte al setup dell'esperimento e all'acquisizione dati, il lavoro principale della mia tesi è stato quello di analizzare la calibrazione in energia dei dati raccolti con tre diverse sorgenti gamma: ^{22}Na, ^{133}Ba and ^{137}Cs. Si è iniziato investigando la qualità dei dati delle forme d'onda raccolte. In seguito è stato fatto uno studio sistematico di analisi di diversi algoritmi per la ricostruzione della carica, selezionando quello più adatto. L'algoritmo scelto è stato poi applicato alla ricostruzione della carica delle sorgenti radioattive e si è ottenuta una curva di calibrazione dell'apparato. Grazie a questa è stato possibile calibrare i dati del fascio di protoni, correggendo lo spettro di energia visibile raccolto dal rivelatore.

Contents

Introduction

1.1 The JUNO experiment

The Jiangmen Underground Neutrino Observatory [1] (JUNO) is the largest state-of-the-art liquid scintillator-based neutrino detector ever constructed. Thanks to its very large mass (20 kton) and demanding performances (3% effective energy resolution at 1 MeV [1]) it will be able to perform important measurements in neutrino physics. JUNO employs an organic Liquid Scintillator (LS) as target for the neutrino interactions. The experiment has been designed [2] to measure the neutrino mass hierarchy using the anti-neutrino produced by the nearby nuclear reactors. Moreover, JUNO will significantly improve the accuracy of the solar neutrinos oscillation parameters and make a significant impact into other neutrino physics topics [1].

The neutrino target is realised with 20 kton of LS. Three components are used in the JUNO LS recipe: Linear Alkyl Benzene (LAB), 2,5-diphenyloxazole (PPO), and 1,4-bis(2-methylstyryl) benzene (bis-MSB). The optimal LS composition was determined to be the purified solvent LAB with 2.5 g/L PPO and 3 mg/L bis-MSB [3].

1.2 The LNL CN beamline setup

The aim of the present thesis is to study the performances of the JUNO LS final recipes with test beam particles.

A small experiment has been designed by the JUNO group lead by Prof. Hans Steineger at the Technische Universität München (TUM), and installed in the beam line of the CN Van-de-Graff accelerator at the INFN National Laboratories in Legnaro (Padua, Italy). The experiment allowed to insert a small setup on the beamline and measure the response of the LS to beam particles.

Figure 1.1 shows a sketch of the beamline and of the detector. The CN accelerator allows to accelerate ion beams (from single protons to $^4He^{++}$ in a pulsed or continuous mode). The ions terminal energy can be varied from about 1 MeV up to 5.5 MeV. The maximum allowed by radioprotection current is about 6 μA in continuos mode and up to 700 nA in pulsed mode at 3 MHz. The data collected during the experiment consists of pulsed proton beams with an energy from 3.5 MeV to 5.5 MeV in steps of 0.5 MeV. As can be seen from Figure 1.1, the protons in the beam hit a thin lithium target (with a thickness of about 20 μm), surrounded by an air-cooled copper (Cu) beam stopper to prevent oxidation of the lithium target. The thickness of the target should be as low as possible, but large enough to have a decent neutron production Because of a higher stopping power, lithium oxide brings lower neutron yields and

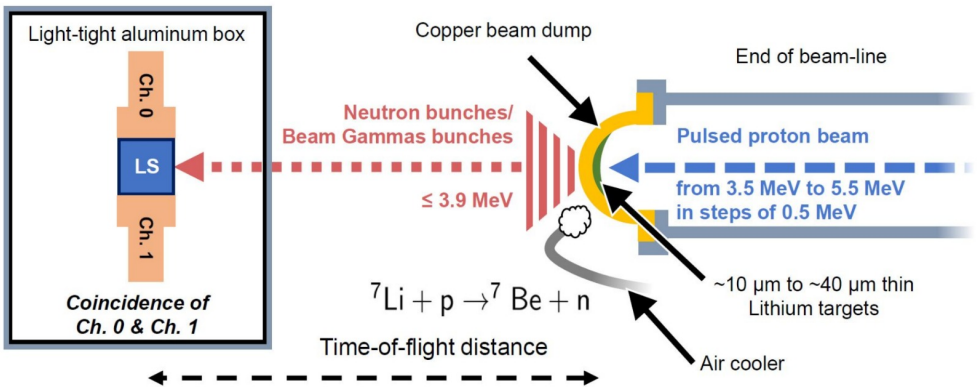

Figure 1.1: Experimental setup of the LNL experiment. Figure taken from [4]

a broadening of the neutron energy spectra. The interactions of the protons proceed with the following nuclear reaction:

$$^7\mathrm{Li} + p \rightarrow ^7\mathrm{Be} + n \tag{1.1}$$

which has a Q-value of -1.644 MeV and a threshold energy of 1.881 MeV [5].

Figure 1.2: Picture of the experimental setup at the CN LNL beamline. A description is given in the text.

A picture of the setup is shown in Figure 1.2. The beam stopper is visible on the left part of the figure, while on the right the 0° setup is visible inside an aluminum box (see also the sketch on the left part of Figure 1.1. The detector is made of a cylindrical ampoule made of glass with an outer diameter of 76 mm and inner diameter of 70 mm) coupled to two 3" photomultiplier tubes (ETEL 9821B). The latter detect the optical photons emitted by the JUNO LS in the scintillation process.

1.3 Energy calibration of the experimental setup

The first important step, before starting to analyse test beam data, has been to calibrate the JUNO-LNL setup with radioactive calibration sources. The following radioactive isotopes have been employed:

- ^{22}Na
- ^{133}Ba
- ^{137}Cs

Table 1.1 reports, for each source, the decay reaction and the energy of the gamma sources. Since the JUNO-LNL setup is quite small and the main interaction process of the emitted photons is Compton effect, the last column of Table 1.1 gives the energy of the recoil electron in the scattering. The energy, E_{CE}, is calculated as

$$E_{CE} = \frac{2E_\gamma^2}{2E_\gamma + m_e c^2} \tag{1.2}$$

where E_γ is the energy of the photon emitted in the decay, while $m_e c^2$ is the electron rest energy. Table 1.1 reports, in the right column, all the E_{CE} energies for the employed sources [6].

source	decay	E_γ [KeV]	E_{CE} [KeV]
^{22}Na	$^{22}Na \overset{\beta^+}{\rightarrow} {}^{22}Ne + \gamma$	1275	1060
	$e^- + e^+ \rightarrow 2\gamma$	511	340
^{133}Ba	$^{133}Ba \overset{\beta^-}{\rightarrow} {}^{133}Cs + \gamma$	356	210
^{137}Cs	$^{137}Cs \overset{\beta^-}{\rightarrow} {}^{137}Ba + \gamma$	662	480

Table 1.1: Overview of the used calibration sources types, their nuclear reactions, decay energies and resulting theoretical Compton edges

In the reconstruction of the recoil electron energy, E_{CE}, the energy resolution of the detector has to be taken into account. The detector response function R takes the form of a Gaussian error function as given in the following formula[4]:

$$\mathrm{R} = \propto \mathrm{erfc}\left(\frac{E - E_{CE}}{\sqrt{2\sigma}}\right) \tag{1.3}$$

Energy calibration runs have been collected before beam measurements: the experimental setup was neither moved nor changed for the calibration apart from the fact that the PMTs high voltage was switched off before placing the source inside the box and then switched on after having closed the setup box.

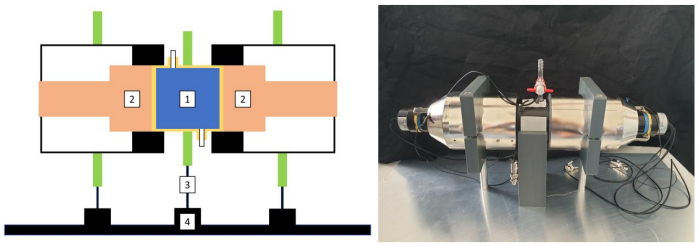

(a) (b)

Figure 1.3: (a) Drawing of the detector which is placed inside the light-tight aluminium dark box. The 3-inch x 3-inch liquid scintillator cell (1), mirrored with aluminium, is coupled to two 3-inch PMTs (2) which are surrounded by mu-metal shields. The setup is held in place by a support structure (3) and mounted onto an aluminium plate (4). (b) A picture of the setup. Taken from [4]

Figure 1.3 shows a detail of the experimental setup inside the box containing the LS vessel and the readout PMTs.

For every radioactive source, a calibration run with 1 million events has been collected. For each of the two readout channels (left and right PMTs), full waveforms have been collected.

Data quality

The present chapter discusses the analysis of the calibration data. The first part consists of quality checks of the collected data in order to verify the reconstructed variables obtained with a `DataProcessor` software described in [4]. We start from the collected waveforms and reconstruct the baseline, the rising and falling times of the signals and, finally, the reconstructed charge.

2.1 General features

Figure 2.1 shows a typical waveform collected during the calibration runs.

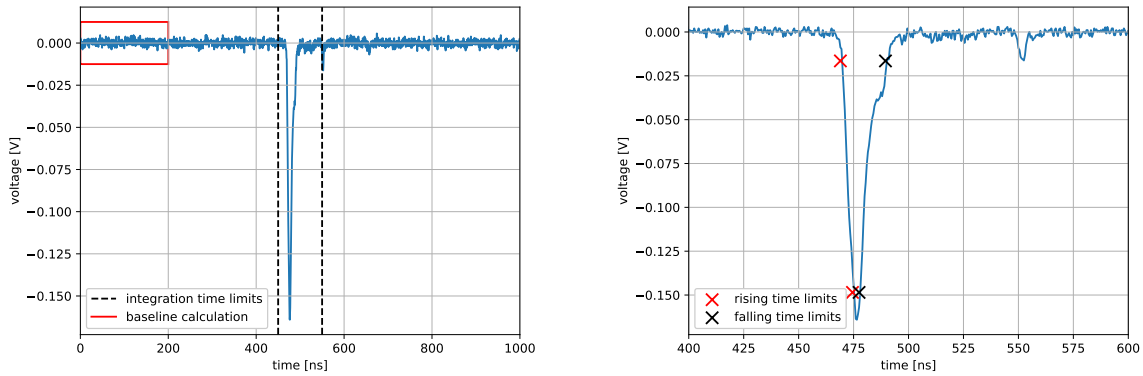

Figure 2.1: Typical waveform collected during a calibration run. Left: the plot shows a full waveform; the region used to compute the baseline and the integrated charge is shown in the picture. Right: a typical waveform with rise-time and fall-time limits superimposed.

The left plot of Figure 2.1 shows, inside a red rectangle, the region used to compute the waveform baseline; the black vertical lines represent the interval used to compute the collected charge. The right plot of the same Figure 2.1 shows the time limits used to compute the rising and falling times of the signal.

The analysis has been performed for both PMTs, here labelled as `channel 1` and `channel 2`; Figure 2.2 shows an example waveform for both PMT channels. The waveforms refer to the same interaction event. Typical waveforms for the other sources (sodium and barium) are reported in the appendix (Figures 7.1 and 7.2, respectively).

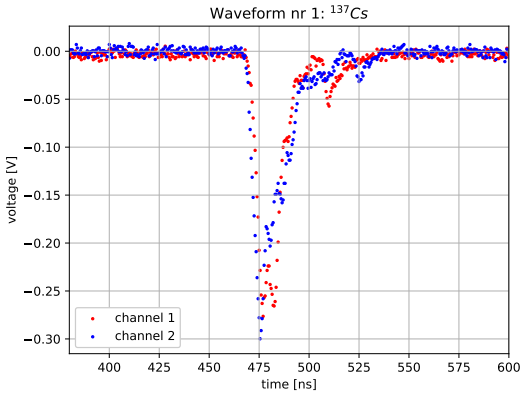

Figure 2.2: Example of a waveform: ^{137}Cs

2.2 Signal baseline

The waveform baseline is computed as the average value of the signal in the first part of the waveform:

$$\text{baseline} = \frac{1}{N}\sum_{i=1}^{N} V_i \ ,$$

where N are the first 100 ns of the waveform (see Figure 2.1).

The next important control parameter is the standard deviation of the noise in the baseline region. This is computed as follows:

$$\sigma = \sqrt{\frac{1}{N-1}\sum_{i=1}^{N}(V_i - \mu)^2} \ , \tag{2.1}$$

and gives an indication of the dispersion of the noise.

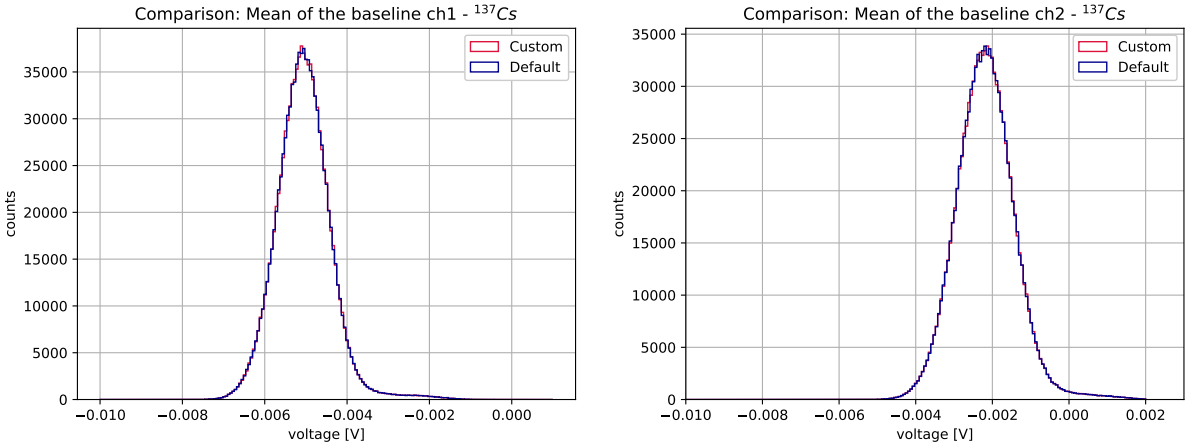

Figure 2.3: Mean of the baseline: ^{137}Cs

The plot of Figure 2.3 shows the distribution of the baseline for all ^{137}Cs collected events. The

two curves are the results obtained by our calculation and the one given by the `DataProcessor` software. The agreement between the two reconstructions is evident.

An important parameter of the distribution is its width computed as

$$FWHM \approx 2 \cdot \sqrt{2 \cdot ln(2)} \cdot \sigma \tag{2.2}$$

where σ is the standard deviation of the distribution (given by eq. (2.1)). The uncertainty on the `FWHM` is given by

$$\sigma_{FWHM} \approx 2 \cdot \sqrt{2 \cdot ln(2)} \cdot s_\sigma \tag{2.3}$$

Both equations 2.2 and 2.3 are valid approximations because the distributions are Gaussian.

The corresponding results for the other used sources are available in the appendix (Figures 7.5 and 7.6).

Table 2.1 reports the FWHM values and uncertainties measured for the used source.

FWHM		^{22}Na [mV]	^{133}Ba [mV]	^{137}Cs [mV]
Waveform data	ch1	2.4232 ± 0.0017	1.5055 ± 0.0011	1.6466 ± 0.0012
	ch2	2.6241 ± 0.0019	1.5110 ± 0.0011	1.8850 ± 0.0013
DataProcessor software	ch1	2.4219 ± 0.0017	1.5051 ± 0.0010	1.6458 ± 0.0012
	ch2	2.6226 ± 0.0019	1.5106 ± 0.0010	1.8840 ± 0.0013

Table 2.1: Measured baseline FWHMs for the used gamma sources.

2.3 Rising and falling times of the signal

The risetime of the signal is computed as the time needed by the signal to go from 10% to 90% of the maximum value.

$$t_R = t_{R90} - t_{R10}$$

Similarly, the falltime is computed as the time needed for going down from 90% to 10% of the signal

$$t_F = t_{F10} - t_{F90}$$

The computation limits are shown in the right plot of Figure 2.1.

The rising and falling times distributions are shown in Figure 2.4 and 2.5 for the ^{137}Cs calibration source. Similar plots, obtained for the other two sources are given in the appendix (Figures 7.3 and 7.4 for the ^{22}Na and ^{133}Ba, respectively).

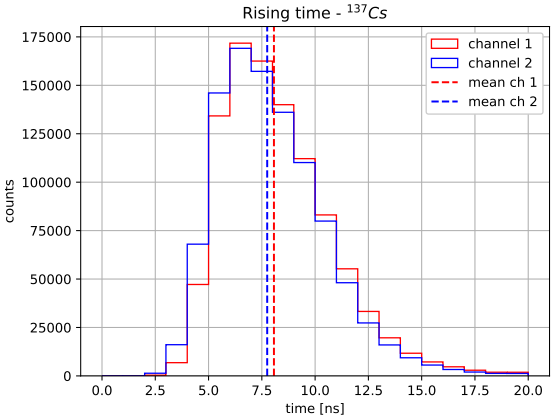

Figure 2.4: Rising time: ^{137}Cs

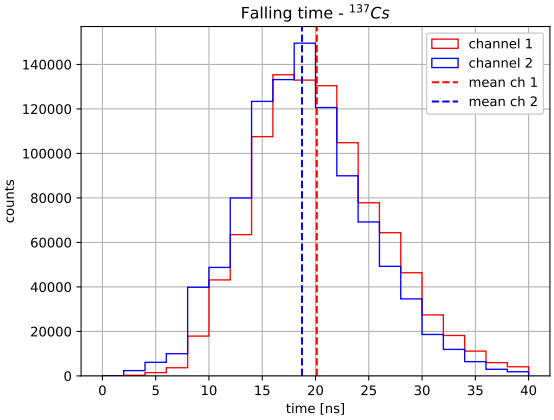

Figure 2.5: Falling time: ^{137}Cs

These plots distributions are the proxies to the form of the waveforms. The average value of the rising time ($t_R \approx 15$ ns) gives us an indication of the fact that the signal increases very rapidly while it takes more time ($t_F \approx 40$ ns) to decrease as expected looking at Figure 2.1.

Charge reconstruction

The integrated charge is the observable closely connected to the energy deposited in the interaction and reconstructed by each PMT (also called visible energy of the interaction). Three different methods have been employed to reconstruct the charge:

- a fixed time interval integral of the signal;
- a variable size window integral, also called Post-pulse Integration Length method (PIL);
- a Continuous Over-Threshold Integral method, called COTI charge reconstruction

Our results have been compared among themselves and also against the charge reconstructed by the `DataProcessor` software. Charge reconstruction is performed separately for the two readout PMTs and the final results given as sum of the two. For each signal, the baseline is subtracted from all channels, as given in

$$I = \sum_{i=t_0}^{t_1} (\mu_{ch1} - V_{ch1,i}) + \sum_{i=t_0}^{t_1} (\mu_{ch2} - V_{ch2,i}) \ , \tag{3.1}$$

where μ_{ch1} and μ_{ch2} are the mean of the waveform baselines for channels 1 and 2, respectively, while t_0 and t_1 are the boundary of the integration.

As described in the following sections, the latters vary, depending on the adopted integration method.

3.1 Fixed window charge integration

The first method is the simplest: for each waveform a fixed time integration window is chosen. A time window between $t_0 = 450$ ns and $t_1 = 550$ ns was selected (see as example the plot in Figure 3.1).

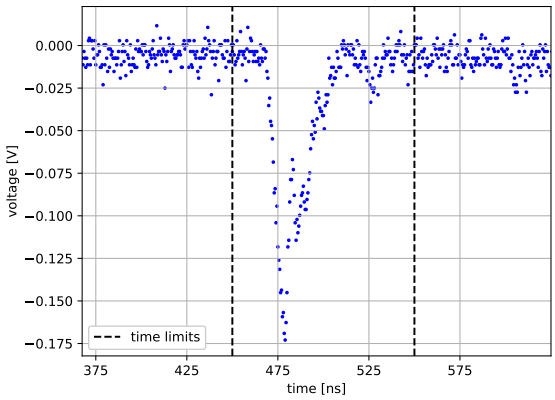

Figure 3.1: Template waveform with fixed limits integration.

3.2 PIL-based charge integration

The second method is an improvement over the first one: the time window over which the integral is computed is not chosen in advance, and can vary for different waveform. The lowest integral limit, t_0, is chosen 40 ns before the time where the signal is at 10% of its lowest value (t_{R10}), while the upper boundary is chosen at an arbitrary but fixed position to the right of t_{R10}. The upper limit of the integral is the so-called post-pulse integration length (PIL) and it is a tunable parameter; in our case we defined it 100 ns after t_{R10}. Figure 3.2 shows our example waveform with the PIL integration limits.

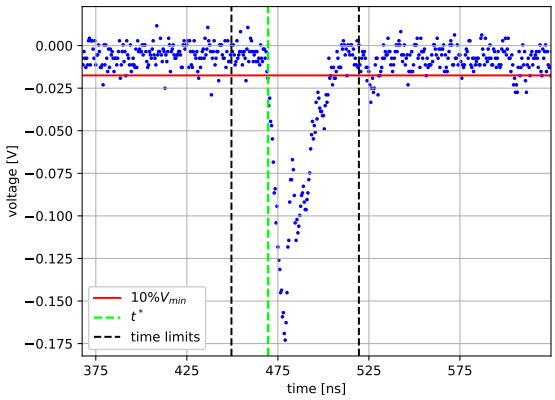

Figure 3.2: Template waveform with PIL-based integration limits.

For our example waveform, 10% of the waveform minimum is around $V_{min} \approx -0.0175\ V$ and it is reached at $t_{R10} \approx 940$ ns. The integration limits are:

$$\begin{aligned} t_0 &= t_{R10} - 40 \text{ ns} \approx 450 \text{ ns} \\ t_1 &= t_{R10} + 100 \text{ ns} \approx 520 \text{ ns} \end{aligned} \tag{3.2}$$

3.3 COTI charge integration

The third charge reconstruction method is the Continuous Over-Threshold Integral (COTI), and the limts of the integral are chosen as follow:

1. starting from the beginning of the waveform, the algorithm selects the first time value where the signal is below the 5σ threshold ;
2. the integral end point is defined by the first time value where the signal becomes smaller than5σ threshold.

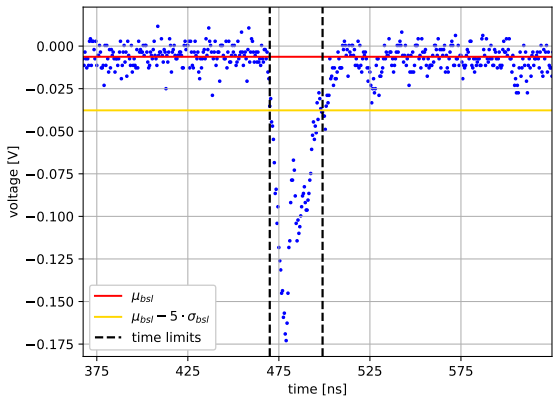

Figure 3.3: Template waveform with COTI charge integration algorithm.

Figure 3.3 gives a graphical representation of the integration interval applied to our template waveform.

$$Q = \sum_{j} (\mu_{bsl} - V_j), \tag{3.3}$$

where $V_j \leqslant \mu_{bsl} - 5\sigma_{bsl}$.

Since COTI algorithm dynamically defines the integration window, the distribution of the left and right time limits can be studied. Figure 3.4 shows a distribution of the left and right time boundaries for the ^{137}Cs calibration data. (The distributions of the COTI time integration limits are given in the appendix for ^{22}Na and ^{133}Ba calibration data in FIgures 7.7 and 7.8, respectively).

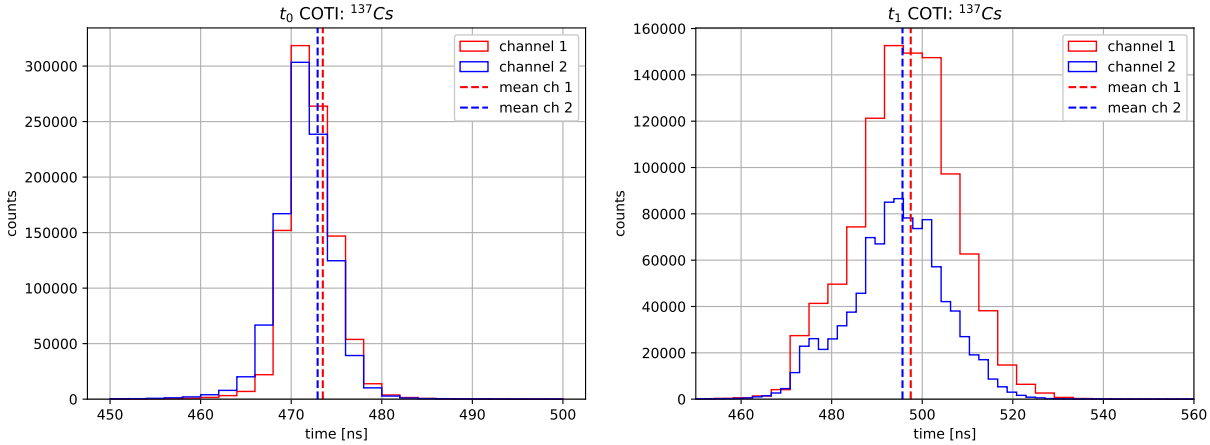

Figure 3.4: COTI times intervals distributions for ^{137}Cs data. Left: lower integral limit. Right: higher integral limit. Distributions are shown for both PMT channels.

The average values of the left time limits are, in the case of cesium,

$$t_{0,ch1} = (4.7 \pm 0.3) \cdot 10^2 \ ns$$
$$t_{0,ch2} = (4.7 \pm 0.3) \cdot 10^2 \ ns$$

while the left limits are, respectively

$$t_{1,ch1} = (5.0 \pm 0.3) \cdot 10^2 \ ns$$
$$t_{1,ch2} = (5.0 \pm 0.3) \cdot 10^2 \ ns$$

Since this choice of the 5σ threshold implies that the time range is smaller, with COTI integration some information is lost and the integrated charged is underestimated with respect to the other two methods.

3.4 Comparison between the different methods

A comparison of the different charge integration methods is shown in Figure 3.5: in addition to the three algorithms described in the previous sections, the result of the `DataProcessor` software is reported. The plot presents for the ^{137}Cs calibration data. (The corresponding plots for the other two calibration sources are given in the appendix in Figures 7.9 and 7.10 for ^{22}Na and ^{133}Ba, respectively).

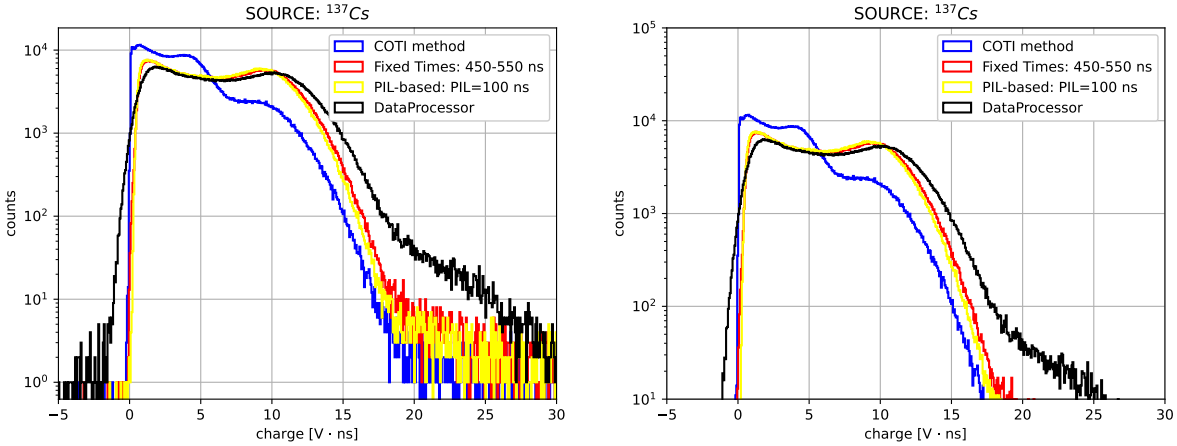

Figure 3.5: Comparison of the different charge integration methods for the ^{137}Cs calibration data. Left: full range plot. Right: zoom on the lower charge values, $Q < 50$ Vs

The fixed times method as well as the PIL-based method provide approximately the same charge estimations as the reference DataProcessor one. On the other hand, the COTI method underestimates the collected charge, because of the strict 5σ condition. On top of that, the COTI method provides an estimation of the left and right limits of the integration. As reported in Figure 3.3, most of the waveforms are within the 450-550 ns boundaries. Therefore, for further analysis, we use the fixed times method with 450-550 ns time limits as the simplest but still reliable method.

The plot of Figure 3.6 shows the charge distribution of the three calibration gamma sources using the fixed times charge integration algorithm.

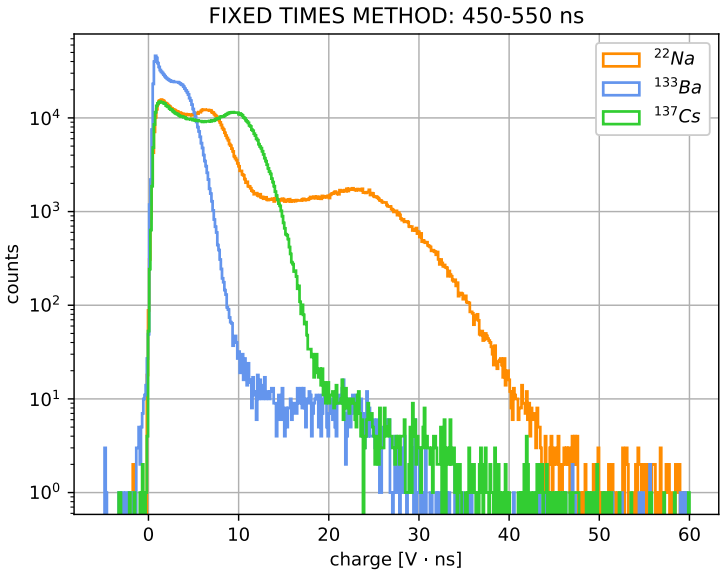

Figure 3.6: Calibration sources energy spectra in the LS detector. The charge has been computed using the fixed times integration window.

Energy calibration

Having reconstructed the total charge, which is proportional to the visible energy of the LS detector, we now proceed in measuring the Compton edges with a fit to the experimental distributions.

4.1 Compton edges fit

In order to determine the position of the Compton edges for each gamma source, a fit to the integrated charge is performed using the complementary error function, *Erfc* [7], given as follows

$$Erfc(x) = \frac{2A}{\pi} \int_{\frac{x-\mu}{\sigma}}^{\infty} e^{-t^2} dt + C \ , \tag{4.1}$$

where μ is the position of the curve half height, corresponding to the estimated position of the Compton edge, σ is a parameter associated to the smearing of the curve (proportional to the resolution of the detector) and A is a normalization constant. Finally, C is a constant shift.

The plot of Figure 4.1 shows the charge spectrum for the ^{137}Cs source; data are fitted to the complementary error function. The charge distributions of the other calibration sources with the fitted curves are available in the appendix in Figure 7.11, 7.12 and 7.13, for the two ^{22}Na gamma values and the ^{133}Ba photon, respectively.

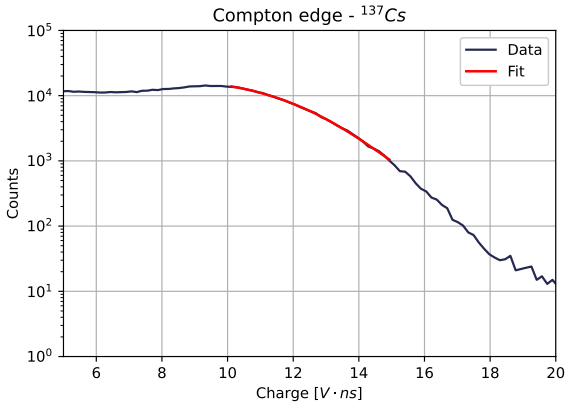

Figure 4.1: Visible energy distribution for the ^{137}Cs data. The plot shows also the complementary error function which is fitted to the data.

$$\mu_{Cs} = (11.74 \pm 0.03) \ V \cdot ns \tag{4.2}$$

4.2 Calibration curve

Having the estimations of the charge related to the Compton edges, we now perform a global linear fit to construct the calibration curve. Table 4.1 summarises the Compton Edges fitted values and the expected values. [1].

source	E_γ [keV]	μ [V ns]	σ [V ns]	E_{CE} [keV]
^{22}Na	511	8.465 ± 0.0011	1.46 ± 0.02	340
^{22}Na	2375	27.74 ± 0.06	5.35 ± 0.12	1060
^{133}Ba	356	4.895 ± 0.008	1.40 ± 0.02	210
^{137}Cs	662	11.74 ± 0.03	2.58 ± 0.05	480

Table 4.1: Results of the Compton edges fits

A linear regression is carried out in order to get the straight line which best approximates the trend of the data and which also gives the integral-energy conversion, needed for the beam data analysis. The results are summarised in figure 4.2 and in table 4.2.

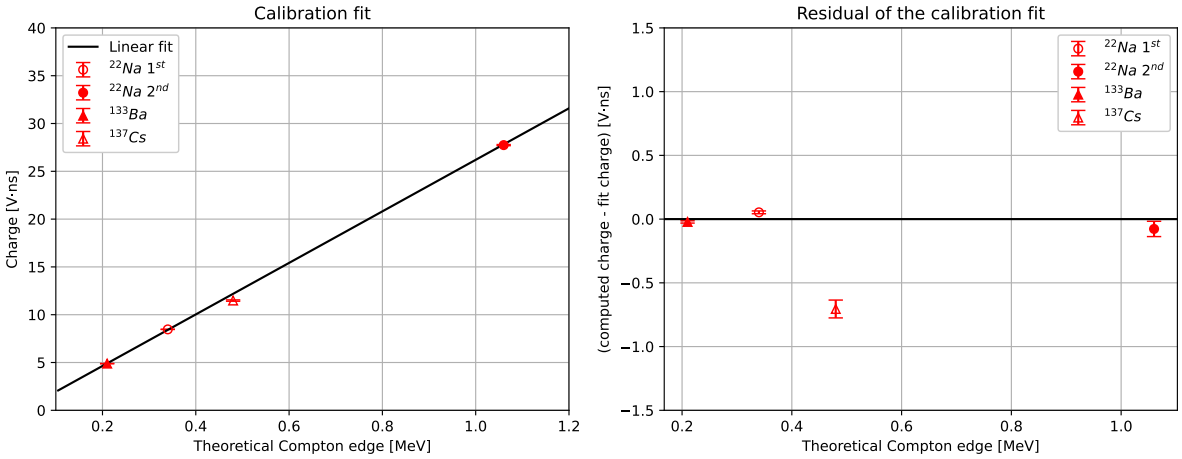

Figure 4.2: Linear regression. Left: calibration fit. Right: residual

$$m = (27.0 \pm 0.6)\ \frac{V \cdot ns}{MeV}$$
$$q = (-0.70 \pm 0.18)\ V \cdot ns$$

Table 4.2: Linear fit parameters

The energy calibration is then used to estimate the visible energy of the beam data, both gammas and neutrons, so a first beam data analysis was done. The plot of Figure 4.3 shows the visible energy of the beam data. The plot includes the contribution of neutrons and gammas.

[1] The Compton edge maximum value is considered without uncertainty.

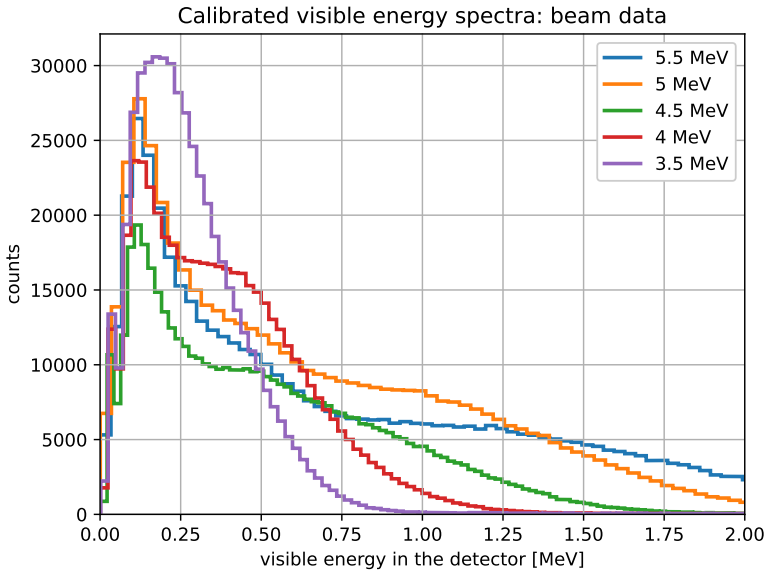

Figure 4.3: Visible energy spectra for the five beam energies used in the experiment. Both gammas and neutrons are shown.

Conclusions

The Jiangmen Underground Neutrino Observatory [1] (JUNO) is the largest state-of-the-art liquid scintillator-based neutrino detector ever constructed. Thanks to its very large mass (20 kton) it will be able to perform important measurements in neutrino physics. The JUNO liquid scintillator is a very important ingredient for the success of the experiment. The goal of the thesis has been to study a sample of the final JUNO LS recipe with test beam particles at the CN proton beam at LNL.

The quality of the collected data has been studied in terms of signal baseline and noise and rising and falling time of the signal waveforms. Afterwards the three different algorithms for calculating the integrated charge has been investigated and compared in details. The energy calibration of the detector has been performed analyzing samples collected with ^{22}Na ^{133}Ba and ^{137}Cs calibration sources. The energy calibration curve has been determined and applied to the beam data.

Acknowledgements

I am very thankful to the TUM group for providing me with the beam data, the `DataProcessor` software, and their guidance during the shifts and the analysis. I'm specially thankful to Prof. Hans Th. J. Steiger for having read my thesis and providing important comments. I am also grateful to Manuel Böhles from the JGU Mainz and Cluster of Excellence Prisma+ for his help both on site and remotely. Finally, I would like to thank Dr. Pierfrancesco Mastinu, Dr. Elizabeth Musacchio and Luca Marran from the Laboratori Nazionali di Legnaro.

Bibliography

[1] A. Abusleme et al. *JUNO physics and detector*. Progress in Particle and Nuclear Physics 123 (2022) 103927. 2023.

[2] Fengpeng An et al. "Neutrino Physics with JUNO". In: *J. Phys. G* 43.3 (2016), p. 030401. DOI: 10.1088/0954-3899/43/3/030401. arXiv: 1507.05613 [physics.ins-det].

[3] A. Abusleme et al. "Optimization of the JUNO liquid scintillator composition using a Daya Bay antineutrino detector". In: *Nucl. Instrum. Meth. A* 988 (2021), p. 164823. DOI: 10.1016/j.nima.2020.164823. arXiv: 2007.00314 [physics.ins-det].

[4] David Jan Dörflinger. "High Precision Measurement of Proton Recoil Quenching". Master thesis. Technische Universität München, 2023.

[5] M. Drosg. "The ^{1}H $(^{7}Li,\ n)$ ^{7}Be reaction as a Neutron source in the MeV range". In: *Los Alamos report, LA-8842-MS UC-34c* (1981).

[6] Hyun Lee et al. "Validation of energy-weighted algorithm for radiation portal monitor using plastic scintillator". In: *Applied Radiation and Isotopes* 107 (Jan. 2016), pp. 160–164. DOI: 10.1016/j.apradiso.2015.10.019.

[7] Riccardo Callegari. "Characterization and tests of 39 channels of the JUNO large PMT electronics". Available at https://thesis.unipd.it/handle/20.500.12608/22810. Master thesis. University of Padova, 2020.

Appendix

Waveforms

The following images show a typical waveform for the same interaction event comparing channel 1 and channel 2 for sodium and barium

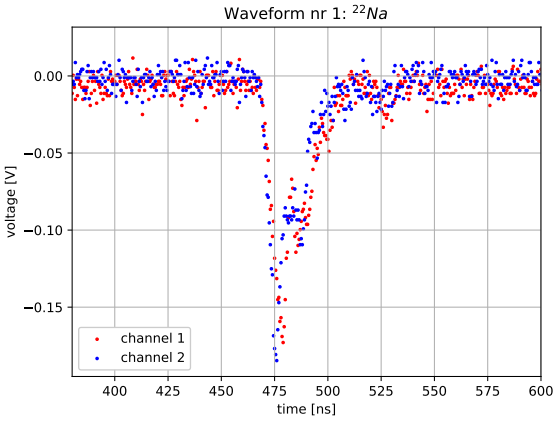

Figure 7.1: Example of a waveform: ^{22}Na

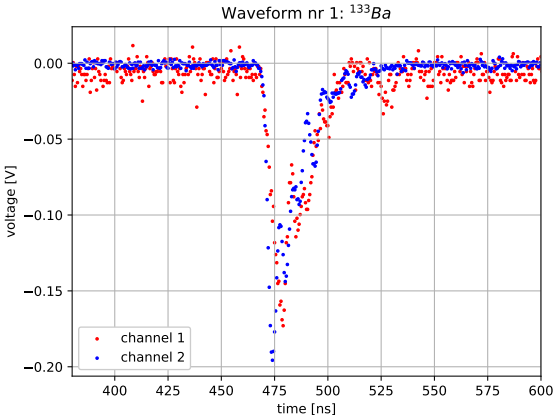

Figure 7.2: Example of a waveform: ^{133}Ba

Rising and falling times

Figures 7.3 and 7.4 show the distribution of the rising times and the falling times for the sodium and barium sources.

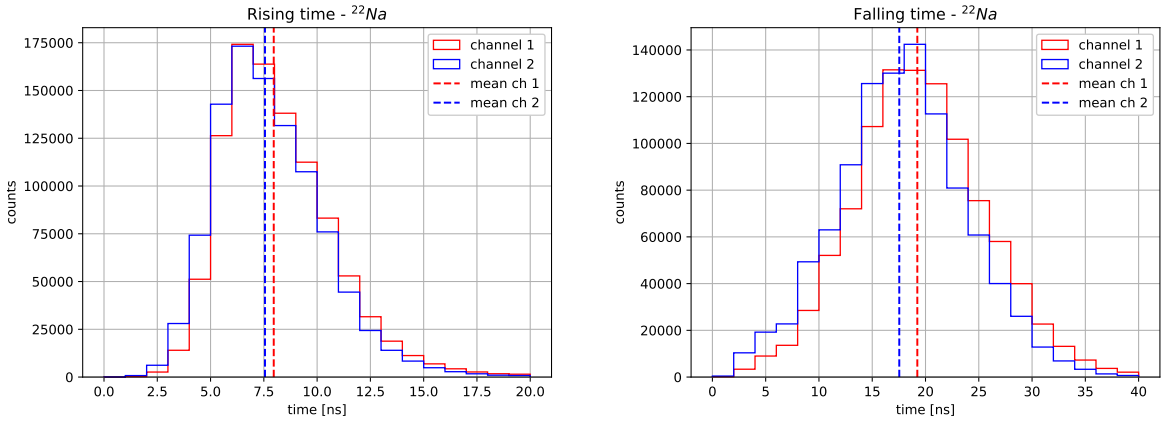

Figure 7.3: Rising and falling times: ^{22}Na

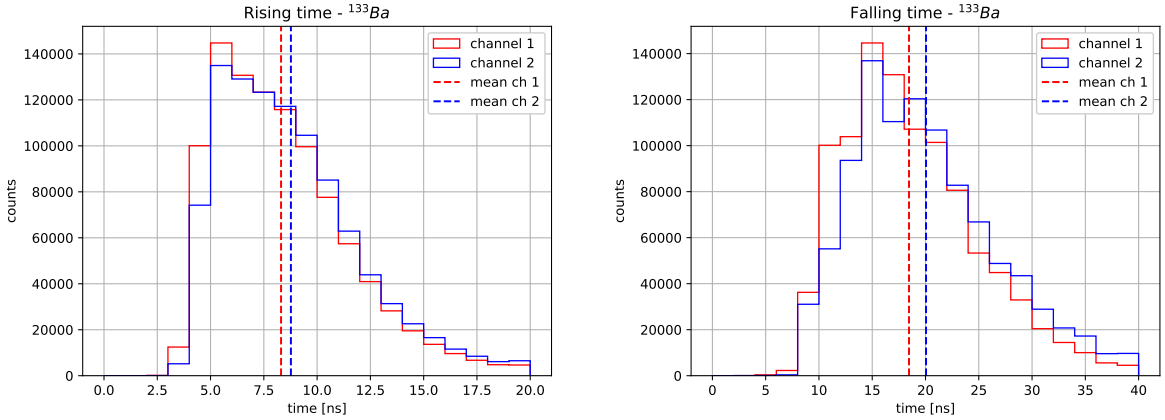

Figure 7.4: Rising and falling time: ^{133}Ba

Baseline

Figures 7.5 and 7.6 show the distribution of the mean of the baseline of the analysed waveforms for the sodium and barium sources.

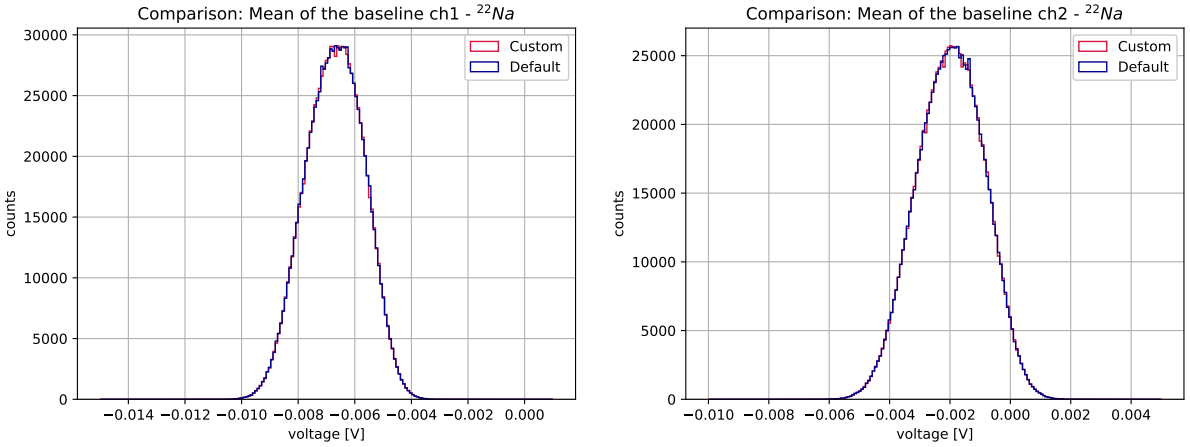

Figure 7.5: Mean of the baseline: ^{22}Na

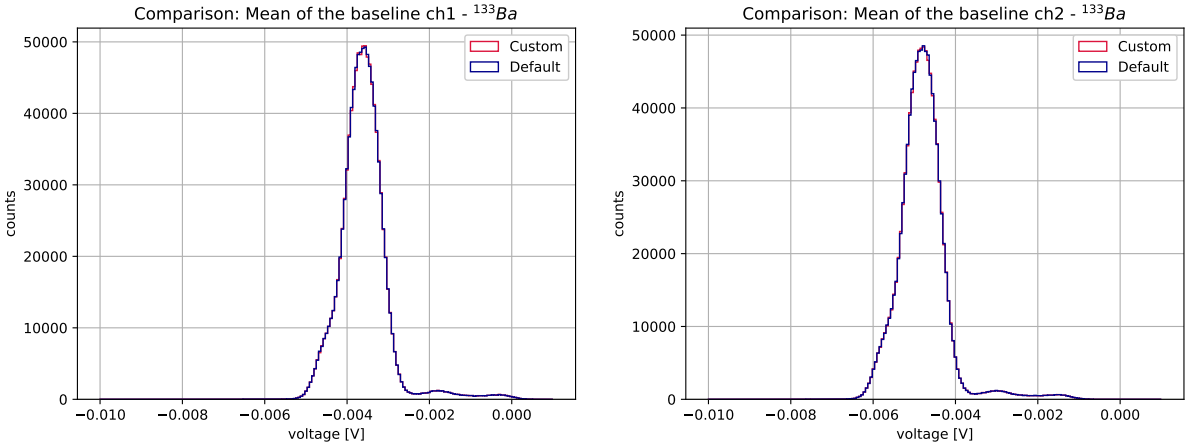

Figure 7.6: Mean of the baseline: ^{133}Ba

COTI times

Figures 7.5 and 7.6 show the distribution of the COTI integration time limits for the sodium and barium sources.

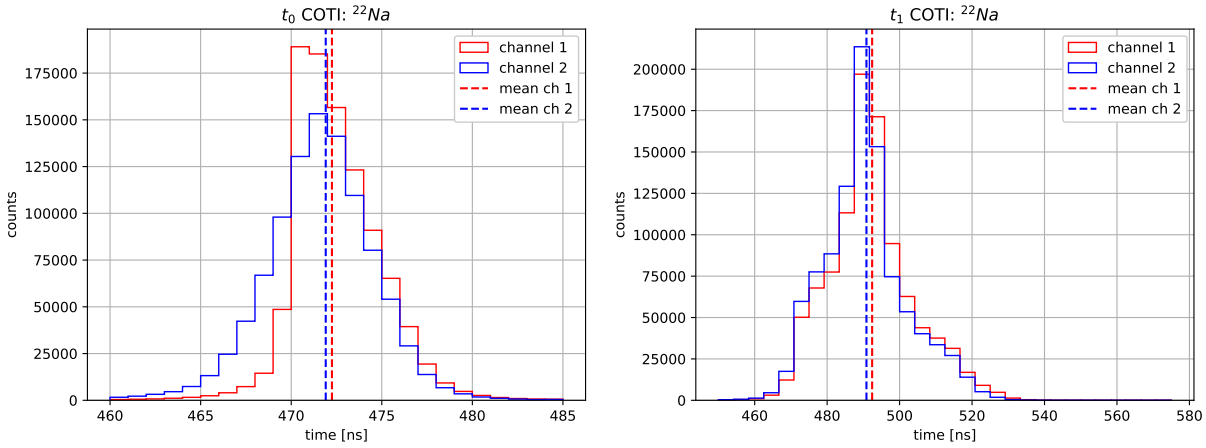

Figure 7.7: COTI time limits: ^{22}Na

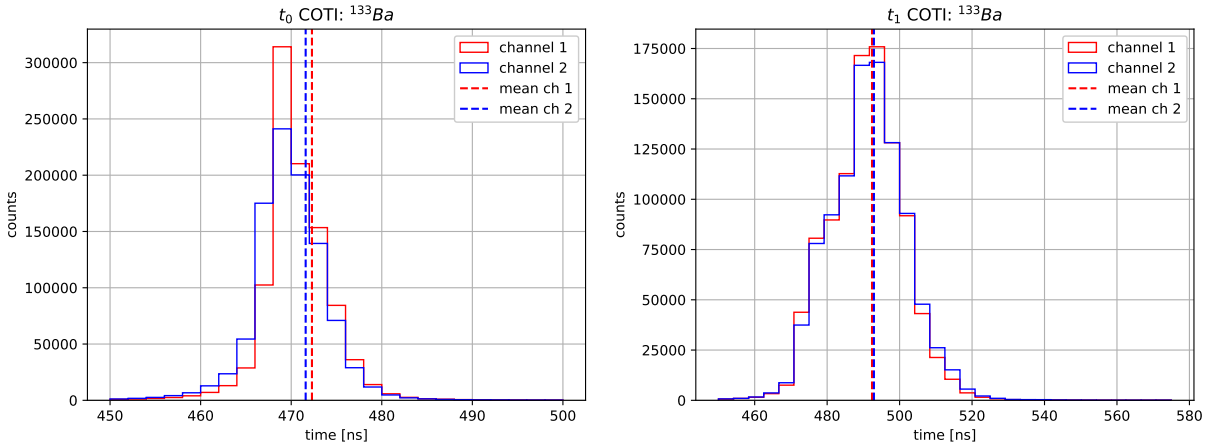

Figure 7.8: COTI time limits: ^{133}Ba

Integrals

Figures 7.9 and 7.10 below show the comparison of the four different charge reconstruction methods for the sodium and barium sources.

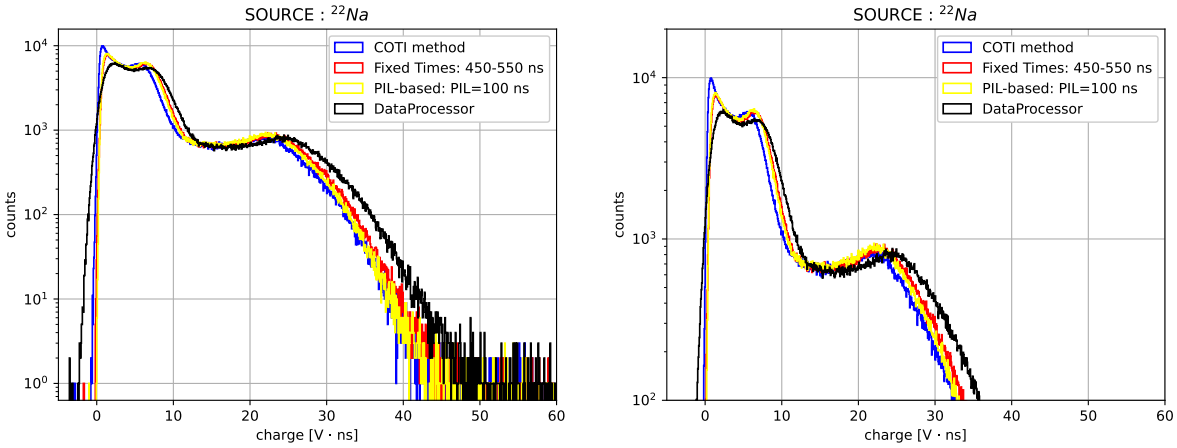

Figure 7.9: Integrals comparison: ^{22}Na

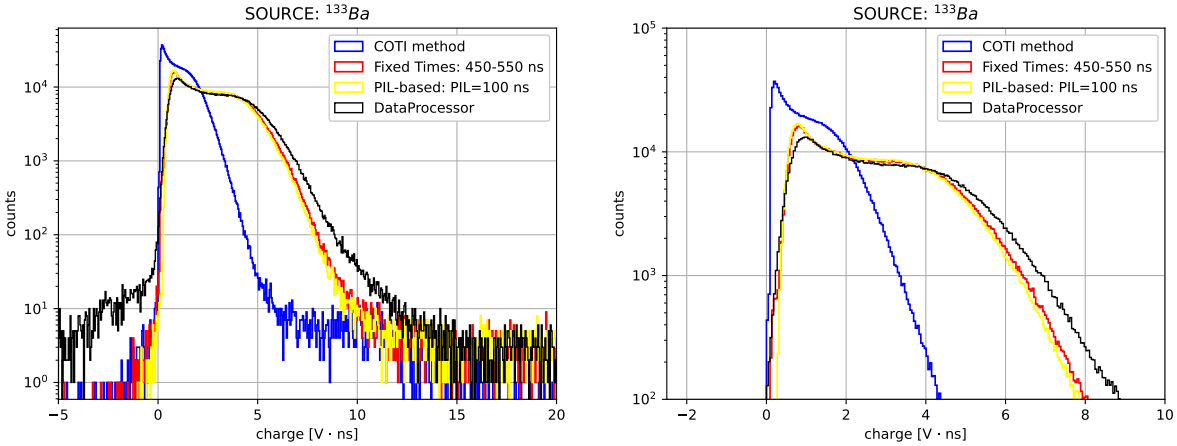

Figure 7.10: Integrals comparison: ^{133}Ba

Compton edges

The first two Figures 7.11 and 7.12 show the fit of the two Compton edges for the sodium source, while Figure 7.13 concerns the Compton edge fit of the barium source.

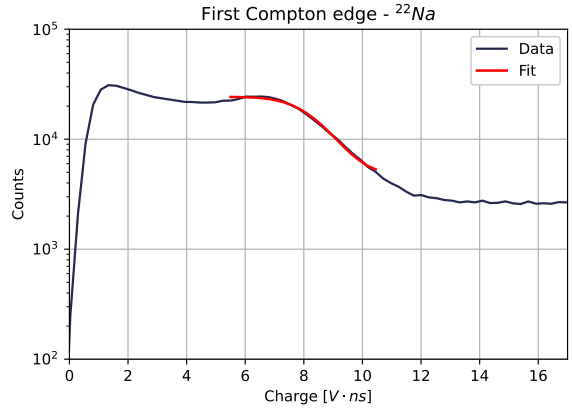

$$\mu_{Na\ 1} = (8.465 \pm 0.011)\ V \cdot ns \tag{7.1}$$

Figure 7.11: First Compton edge fit: ^{22}Na

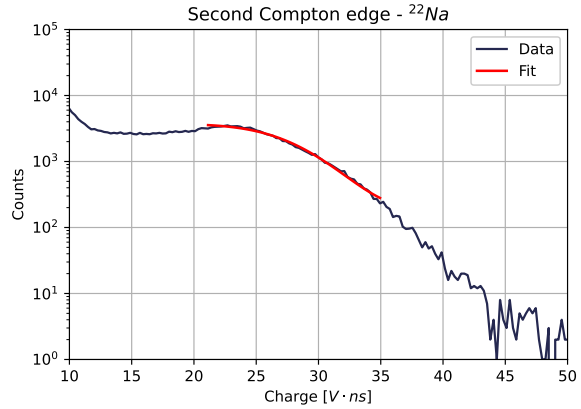

$$\mu_{Na\ 2} = (27.74 \pm 0.06)\ V \cdot ns \tag{7.2}$$

Figure 7.12: Second Compton edge fit: ^{22}Na

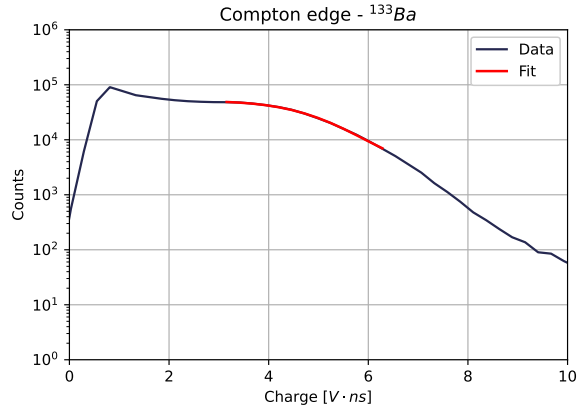

$$\mu_{Ba} = (4.895 \pm 0.008)\ V \cdot ns \tag{7.3}$$

Figure 7.13: Compton edge fit: ^{133}Ba